University of Reading

On the origin of the sudden heliospheric open magnetic flux enhancement during the 2014 pole reversal

Article

Published Version

Creative Commons: Attribution 4.0 (CC-BY)

Open Access

Heinemann, S. G. ORCID: https://orcid.org/0000-0002-2655-2108, Owens, M. J. ORCID: https://orcid.org/0000-0003-2061-2453, Temmer, M. ORCID: https://orcid.org/0000-0003-4867-7558, Turtle, J. A., Arge, C. N. ORCID: https://orcid.org/0000-0001-9326-3448, Henney, C. J. ORCID: https://orcid.org/0000-0002-6038-6369, Pomoell, J. ORCID: https://orcid.org/0000-0003-1175-7124, Asvestari, E. ORCID: https://orcid.org/0000-0002-6998-7224, Linker, J. A. ORCID: https://orcid.org/0000-0003-1662-3328, Downs, C. ORCID: https://orcid.org/0000-0003-1759-4354, Caplan, R. M. ORCID: https://orcid.org/0000-0002-2633-4290, Hofmeister, S. J. ORCID: https://orcid.org/0000-0001-7662-1960, Scolini, C. ORCID: https://orcid.org/0000-0002-5681-0526, Pinto, R. F. ORCID: https://orcid.org/0000-0001-8247-7168 and Madjarska, M. S. ORCID: https://orcid.org/0000-0001-9806-2485 (2024) On the origin of the sudden heliospheric open magnetic flux enhancement during the 2014 pole reversal. The Astrophysical Journal, 965 (2). 151. ISSN 0004-637X doi: 10.3847/1538-4357/ad2b69 Available at https://centaur.reading.ac.uk/116080/

University of Reading

It is advisable to refer to the publisher's version if you intend to cite from the work. See Guidance on citing.

To link to this article DOI: http://dx.doi.org/10.3847/1538-4357/ad2b69

Publisher: American Astronomical Society

All outputs in CentAUR are protected by Intellectual Property Rights law, including copyright law. Copyright and IPR is retained by the creators or other copyright holders. Terms and conditions for use of this material are defined in the End User Agreement.

www.reading.ac.uk/centaur

CentAUR

Central Archive at the University of Reading

Reading's research outputs online

The Astrophysical Journal, 965:151 (10pp), 2024 April 20 https://doi.org/10.3847/1538-4357/ad2b69
© 2024. The Author(s). Published by the American Astronomical Society.
OPEN ACCESS

On the Origin of the Sudden Heliospheric Open Magnetic Flux Enhancement During the 2014 Pole Reversal

Stephan G. Heinemann[1], Mathew J. Owens[2], Manuela Temmer[3], James A. Turtle[4], Charles N. Arge[5], Carl J. Henney[6], Jens Pomoell[1], Eleanna Asvestari[1], Jon A. Linker[4], Cooper Downs[4], Ronald M. Caplan[4], Stefan J. Hofmeister[7], Camilla Scolini[8,9], Rui F. Pinto[10], and Maria S. Madjarska[11,12]

[1] Department of Physics, University of Helsinki, P.O. Box 64, 00014, Helsinki, Finland; stephan.heinemann@hmail.at
[2] Space and Atmospheric Electricity Group, Department of Meteorology, University of Reading, Earley Gate, P.O. Box 243, Reading, RG6 6BB, UK
[3] Institute of Physics, University of Graz, Universitätsplatz 5, 8010 Graz, Austria
[4] Predictive Science Inc., 9990 Mesa Rim Road, Suite 170, San Diego, CA 92121, USA
[5] Heliophysics Science Division,NASA Goddard Space Flight Center, Code 671, Greenbelt, MD 20771, USA
[6] Air Force Research Laboratory, Space Vehicles Directorate, KAFB, NM 87117, USA
[7] Leibniz-Institute for Astrophysics Potsdam, An der Sternwarte 16, 14482 Potsdam, Germany
[8] Institute for the Study of Earth, Oceans, and Space, University of New Hampshire, Durham, NH 03824, USA
[9] Solar–Terrestrial Centre of Excellence–SIDC, Royal Observatory of Belgium, 1180 Uccle, Belgium
[10] IRAP, Université de Toulouse; UPS-OMP; CNRS, 9 Av. colonel Roche, BP 44346, F-31028 Toulouse cedex 4, France
[11] Max-Planck-Institut für Sonnensystemforschung, Justus-von-Liebig-Weg 3, 37077 Göttingen, Germany
[12] Space Research and Technology Institute, Bulgarian Academy of Sciences, Acad. Georgy Bonchev Str., Bl. 1, 1113, Sofia, Bulgaria
Received 2023 November 10; revised 2024 February 16; accepted 2024 February 19; published 2024 April 16

Abstract

Coronal holes are recognized as the primary sources of heliospheric open magnetic flux (OMF). However, a noticeable gap exists between in situ measured OMF and that derived from remote-sensing observations of the Sun. In this study, we investigate the OMF evolution and its connection to solar structures throughout 2014, with special emphasis on the period from September to October, where a sudden and significant OMF increase was reported. By deriving the OMF evolution at 1 au, modeling it at the source surface, and analyzing solar photospheric data, we provide a comprehensive analysis of the observed phenomenon. First, we establish a strong correlation between the OMF increase and the solar magnetic field derived from a potential-field source-surface model ($cc_{\mathrm{Pearson}} = 0.94$). Moreover, we find a good correlation between the OMF and the open flux derived from solar coronal holes ($cc_{\mathrm{Pearson}} = 0.88$), although the coronal holes only contain 14%–32% of the Sun's total open flux. However, we note that while the OMF evolution correlates with coronal hole open flux, there is no correlation with the coronal hole area evolution ($cc_{\mathrm{Pearson}} = 0.0$). The temporal increase in OMF correlates with the vanishing remnant magnetic field at the southern pole, caused by poleward flux circulations from the decay of numerous active regions months earlier. Additionally, our analysis suggests a potential link between the OMF enhancement and the concurrent emergence of the largest active region in solar cycle 24. In conclusion, our study provides insights into the strong increase in OMF observed during 2014 September–October.

Unified Astronomy Thesaurus concepts: Solar magnetic fields (1503); Solar physics (1476); Heliosphere (711)

1. Introduction

The Sun continuously releases magnetized plasma into heliospheric space, which is commonly known as the solar wind. The outflowing solar wind plays a key role by shaping the heliospheric medium and providing the ambient structure in which solar transients, such as coronal mass ejections (CMEs), propagate (see review by Temmer 2021, and references therein). The solar wind can be roughly differentiated into two populations, slow and fast solar winds.

The sources of the slow wind are still strongly debated (see Viall & Borovsky 2020 for open questions about solar wind sources). One class of theories argues that the slow wind predominantly arises quasi-statically from regions of large expansion factor at the boundaries of coronal holes, while other theories argue that it arises primarily from interchange reconnection (see Abbo et al. 2016, and references therein). This includes reconnection on top of closed loops, separatrix structures, or interchange reconnection. Regions where these processes may occur are manifold, such as photospheric magnetic field with a web-like network ("S-web"; Antiochos et al. 2011), quiet-Sun regions (Fisk et al. 1998), smaller equatorial coronal holes (Bale et al. 2019; Stansby et al. 2020), coronal hole boundaries (Wang & Sheeley 1990; Owens et al. 2018; Macneil et al. 2020), edges of active regions (Sakao et al. 2007; Doschek et al. 2008; Harra et al. 2008), and coronal- and pseudo-streamers (Ofman 2004; Riley & Luhmann 2012).

The fast wind is believed to originate in the core of the regions where the open solar magnetic field is rooted, along which the plasma is accelerated into the heliospheric space. These large-scale regions are often observed as regions of reduced emission EUV and X-ray (on-disk), white-light (off-limb) or as bright structures in He I10830 Å (see, e.g., Bohlin 1977; Hofmeister et al. 2017; Heinemann et al. 2019a). The prevalence of coronal holes aligns with the solar activity cycle, where large coronal holes cover the poles in times of low solar activity and smaller equatorial coronal holes are seen during solar maximum (Cranmer 2009; Hewins et al. 2020). Although equatorial coronal holes can be found during solar minimum, in contrast to solar maximum they are found to

Original content from this work may be used under the terms of the Creative Commons Attribution 4.0 licence. Any further distribution of this work must maintain attribution to the author(s) and the title of the work, journal citation and DOI.

feature more diffuse and fragmented boundaries ("patchy" coronal holes; Heinemann et al. 2020; Samara et al. 2022). Being regions intrinsically linked to regions of open field, coronal holes are expected to be the primary source of the heliospheric open flux throughout the solar cycle.

Recent studies have revealed a significant discrepancy between the heliospheric open magnetic flux (OMF) derived from remote sensing (typically through potential field modeling) and the heliospheric OMF measured in the heliosphere at 1 au, which is known as the "open flux problem" (Wang & Sheeley 1995; Wang et al. 2000; Linker et al. 2017; Wallace et al. 2019). Linker et al. (2017) found a difference of more than a factor 2, and Linker et al. (2021) suggested multiple sources of uncertainty in the determination of the open flux. However, even when considering the uncertainties, the missing open flux cannot be accounted for. And despite the persistent discrepancy, the trend between the in situ measured heliospheric and the open flux based on remote-sensing observations seems to be roughly correlated. Yoshida et al. (2023) suggested that the change in open solar flux is related to the evolution and interaction between the dipole and the nondipole components of the global field. Arge et al. (2024) proposed that active regions located near the boundaries of midlatitude coronal holes could be a possible source of the missing open flux. By considering active regions in close proximity to coronal holes as an additional source of open flux, their results show good agreement over 27 yr of data with the in situ measured OMF. However, the missing flux has yet to be definitively accounted for.

The evolution of the OMF seems to roughly follow the solar cycle (Owens & Forsyth 2013). Even when using improved and sophisticated algorithms to calculate the best estimate of the OMF, it yields results that raise questions about certain changes in the OMF profile that seem not to match the global solar surface structure evolution. Frost et al. (2022) derived the evolution of the OMF including uncertainty estimates, from 1995 to 2021, and identified a sudden increase in heliospheric OMF around 2014 September–October. They find that within a few solar rotations the OMF at 1 au increased by over a factor of 2. This large, rapid change in OMF is a useful marker that may be exploited to connect and understand the temporal variations in photospheric, coronal, and interplanetary magnetic fields.

In this study, we aim to trace the sudden enhancement of the OMF back to its solar origin in order to uncover its source. We derive the OMF evolution at 1 au, and compare that to the modeled one at the source surface and at the solar photosphere using coronal hole observations. In addition, we examine the dynamic evolution of the solar magnetic field in 2014 in relation to emergence and decay of solar coronal holes and active regions. Thereby, we aim to shed light on solar processes that enable the opening of a large amount of magnetic flux in a short period of time relative to that of solar cycles.

2. Methods

To derive the evolution of the OMF and its source, we investigate the magnetic field structure of the Sun by combining different techniques and data products at various heliocentric distances.

Table 1
CHMAP Extraction Parameters

Parameter	Caplan et al. (2016) $\log_{10}(I)$	This Study $\log_{10}(I)$
Seeding threshold	0.95	1.05
Outer threshold	1.35	1.50

2.1. Coronal Holes

Assuming that the majority of the open flux originates in solar coronal holes, our primary focus is to accurately determine the area and associated magnetic flux of all coronal holes from 2014 June to December. To observe the full 360° of the Sun, we make use of the optimal positioning of the Solar TErrestrial RElations Observatories (STEREOs; Kaiser et al. 2008) and the Solar Dynamics Observatory (SDO; Pesnell et al. 2012), whose combined field of view covers nearly the full Sun during the time period of interest. For this, we use the Coronal Hole Mapping and Analysis Pipeline (CHMAP) open-source Python software package[13]. 195 Å filtergrams from the Extreme UltraViolet Imager (Wuelser et al. 2004) on board STEREO-A(head) and B(ehind) and 193 Å filtergrams from the Atmospheric Imaging Assembly (Lemen et al. 2012) on board SDO are integrated in CHMAP into a single, synchronic Carrington map including automated coronal hole detections. To ensure their high quality, the individual images from each spacecraft are deconvolved, corrected for limb brightening and cross-calibrated. After the images from different instruments are cross-calibrated, the coronal hole detection algorithm is applied. An iterative, kernel-based two-threshold scheme is used, where one (lower-) intensity threshold is employed for seeding the coronal holes and a second (higher-) intensity threshold for defining the boundaries (Caplan et al. 2016). The original detection parameters in Caplan et al. (2016) were manually chosen primarily based on visual inspection and comparison to the EUV data for the period of 2012–2014. For this study, we used an updated and improved set of parameters to minimize the underdetection of coronal holes, at the expense of sometimes including filament channels. The extraction parameters were updated based on visual inspection and comparison to reliable coronal hole extractions of individual coronal holes (using CATCH; Heinemann et al. 2019a). As the filament channels have nearly balanced flux, these overdetections contribute very little to the open flux estimate (see Table 1). The seeds are then iteratively grown until the kernel and/or upper threshold are met at all coronal hole edges. The coronal hole detection is performed on individual full-disk images and only interpolated to Carrington maps (4096×2048 pixels) afterwards. This results in one map for each timestamp and each instrument. Using a minimum-intensity merge Caplan et al. (2023) procedure, we combine these maps into single synchronic maps. Lastly, the map resolution was reduced by integration to 1080×540 pixels, and then further binned to a 1° resolution, matching that used in the magnetic field maps. An example is shown in Figure 1, top panel.

2.2. Surface Open Flux

As the STEREO spacecraft do not provide magnetic field remote observations, we must rely on time-dependent

[13] http://github.com/predsci/CHMAP

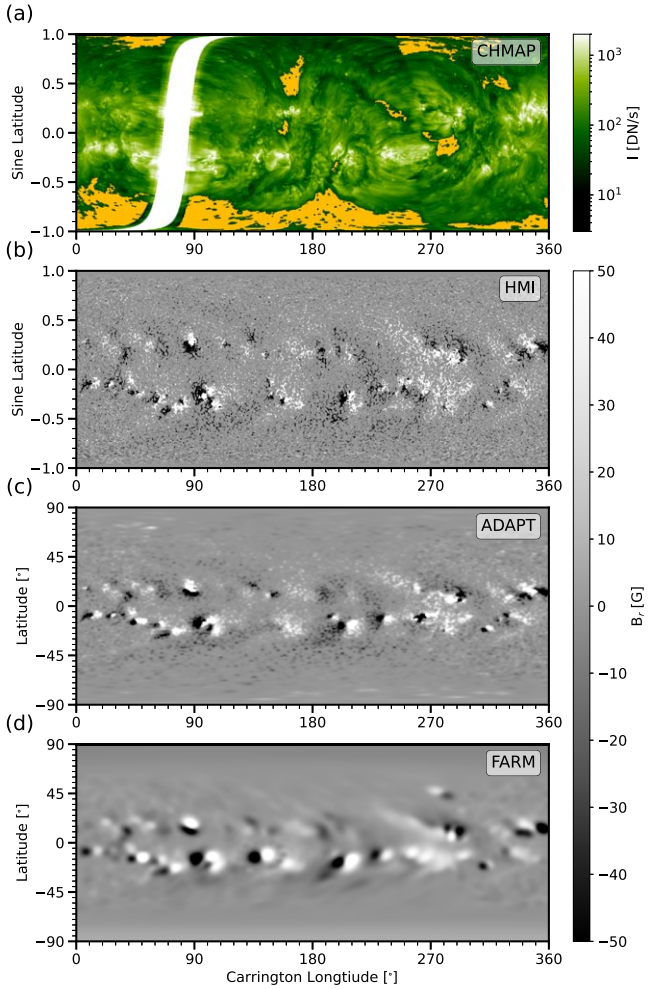

Figure 1. State of the Sun on 2014 September 19, as viewed from different perspectives. From top to bottom: CHMAP EUV chart with the corresponding coronal hole traction overlaid in yellow, HMI pole-filled daily synoptic chart, HMI-ADAPT magnetogram, and FARM magnetogram.

observations obtained solely along the Earth–Sun line to derive the magnetic field over the entire surface. To include the uncertainties in the magnetic field observations due to calibration and the "aging effect" (Heinemann et al. 2021), we make use of three different magnetograms. First, we use magnetograms from the Helioseismic and Magnetic Imager (HMI; Schou et al. 2012) combined to the standard data product `hmi.mrdailysynframe_polfil_720s` available via the Joint Science Operations Center (JSOC).[14] Second, for compensating (up to some extent) for the evolution of solar magnetic fields during one solar rotation, we use HMI magnetic field data assembled by the Air Force data assimilative photospheric flux transport (ADAPT) model (see, e.g., Arge et al. 2013; Hickmann et al. 2015; Barnes et al. 2023). Note that the flux-scaling method used by these ADAPT maps ($B_{scale} = 1.86576$) was factored out so that the magnetic field values are consistent with the other magnetograms used. Lastly, we use magnetograms from the combined surface flux transport and helioseismic Far-side Active Region Model (FARM; Yang et al. 2024) that features far-side active regions detected by helioseismic holography (Yang et al. 2023), which are then added to an HMI-based surface flux transport model (derived from Baumann 2005) to give a more temporally accurate representation of the solar surface magnetic field. Examples of these maps are shown in the lower panels in Figure (1). All three magnetogram data products were used at a 1 day cadence to match the time cadence of the coronal hole extractions. By binning to a 1° resolution and coalignment of the magnetic maps and the coronal hole observation, the coronal hole boundaries can be projected to the photosphere, thus allowing one to compute the signed magnetic field density (B_{ch}) and to extract the signed magnetic flux (Φ_{ch}). For each day, the total coronal hole flux is computed as

$$\Phi_{\odot} = \sum_i |\Phi_{CH,i}|, \quad (1)$$

with i subscripting every coronal hole at a given time. Note that no radial scaling to 1 au is required for comparison with the total OMF derived from in situ observations as the radial field magnitude decreases by r^{-2} for an ideal Parker spiral and the area, respectively, increases by r^2.

2.3. Source-surface Open Flux

The OMF was calculated using a potential-field source-surface (PFSS) magnetic field model (Altschuler & Newkirk 1969) based on a finite-difference scheme. It solves a discrete Laplace equation for the scalar potential by employing a staggered representation for the magnetic field. This ensures that the magnetic field has exactly (to floating-point accuracy) zero divergence and curl in the discrete representation. In addition, the input magnetogram is exactly reproduced by the model. We note that, as shown in Caplan et al. (2021), open flux calculations from PFSS models are nearly resolution independent, allowing us to use the 1° map resolution reliably. Early studies (e.g., Altschuler & Newkirk 1969; Hoeksema 1984) suggested that an optimal source surface is placed around $R_{ss} = 2.5\ R_{\odot}$, which has since become recognized as the standard height. However, it is generally acknowledged that a fixed source-surface height does not always yield reliable results but may need to be modified according to the coronal configuration. McGregor et al. (2008) varied their source-surface height between 2.0 and 2.6R_s, and Asvestari et al. (2019) used 1.4–3.2 R_s. This probes the coronal range in which the source surface still opens a significant amount of closed loops (lower boundary) and only opens large-scale open flux concentrations (upper boundary). Our six source-surface heights were chosen to map this parameter domain. However, Asvestari et al. (2019) showed that the agreement between observed coronal hole areas and PFSS open field is strongly dependent on the choice of the source-surface height for individual coronal holes. Per definition, a lower source-surface height leads to an increase in the modeled open flux. To account for this, we calculate the model flux using all three different magnetograms and employing six different source-surface heights set at $R_{ss} = [1.6, 1.9, 2.2, 2.5, 2.8, 3.1]\ R_{\odot}$ to constrain the derived open flux at very low and very high source-surface heights. Thus, for every model realization we compute the open flux at the source surface as

$$\Phi_{PFSS},\ R_{ss} = \sum_j |\Phi_{R_{ss},j}|, \quad (2)$$

where $|\Phi_{R_{ss},j}|$ denotes every pixel at a given source surface. To easily demonstrate the trend over time, we derive a single time series computed from the mean flux from the six derived fluxes

[14] http://jsoc.stanford.edu/

with the upper and lower boundaries constrained by the highest and lowest source surface ($R_{ss} = 1.6$ and 3.1 $R_\odot$, respectively):

$$\Phi_{\mathrm{PFSS}} = \frac{1}{6} \sum_{R_{ss}=1.6}^{3.1} \Phi_{R_{ss}}. \quad (3)$$

Even though we calculate an average of the PFSS curves for the open flux that covers the full range of commonly used source-surface values, it can be used to derive trends but might not be reliable for individual events. For such events, the specific results should be examined.

2.4. Heliospheric Open Flux

From magnetic field data taken by the Ulysses spacecraft, Suess et al. (1996) and Suess & Smith (1996) showed that the magnitude of heliospheric magnetic field ($|B_r|$) is independent of latitude. With this assumption, the longitudinal coverage can be obtained by integrating the in situ measured total magnetic field over one solar rotation, and further the total OMF can be calculated as $\Phi_{OMF} = 4\pi R^2 \langle |B_r| \rangle$, where R is the respective solar distance of the observations and $\langle |B_r| \rangle$ the 27 days average. However, this method has uncertainties related to the time resolution over which the modulus is computed. It affects how effectively small-scale inversions in B_r flux (also called "folded flux") are averaged out (Owens et al. 2017). Choosing the averaging interval to be too short will lead to the inclusion of locally inverted B_r structures at 1 au which are not present at the source surface. Too long of an averaging interval will cancel B_r across the heliospheric current sheet and hence remove B_r structures at 1 au which are present at the source surface. In practice, this optimum time averaging will vary, particularly over the solar cycle. Instead, we use the suprathermal electron strahl to determine whether magnetic flux connects directly to the source surface, or whether it is locally inverted (Owens et al. 2017).

The OMF is derived from in situ measurements obtained by the Advanced Composition Explorer (ACE; Stone et al. 1998) and Wind (Acuña et al. 1995) as stated by Frost et al. (2022). Magnetic Field Monitor (Smith et al. 1998) data are utilized to determine the orientation of the heliospheric magnetic field, while electron data from the Solar Wind Electron, Proton, and Alpha Monitor (McComas et al. 1998) are used. For Wind, data from the Magnetic Field Investigation (Lepping et al. 1995) and the 3DP Plasma Analyzer (Lin et al. 1995) are utilized. Detection of the strahl involves automatic identification of an increase in electron flux at 0° or 180° pitch angle, exceeding 50% of the background flux (determined as the flux at 90° pitch angle) in the 292 eV energy channel. If neither enhancement is present, it indicates the absence of the strahl (sometimes referred to as a heat flux dropout). In cases where both 0 and 180 strahl are detected, the interval is classified as counterstreaming (indicative of closed flux in the heliosphere) if the strahl fluxes are within a factor of 2 of each other. Otherwise, if one strahl flux exceeds twice the other, the strahl direction is determined by the highest flux. These criteria were established by comparing with previous counterstreaming and heat flux dropout occurrence rates reported in studies conducted visually (Gosling et al. 1992; Skoug et al. 2000; Pagel et al. 2005; Anderson et al. 2012). Uncertainties are determined through cross-comparison between ACE and Wind data, as well as data gap analysis. They are computed as a percentage interpolation of the 90% confidence intervals provided in Frost et al. (2022) to our data set, aiming to establish a lower bound of the uncertainty. Over our time period, this uncertainty amounts to approximately ±5%.

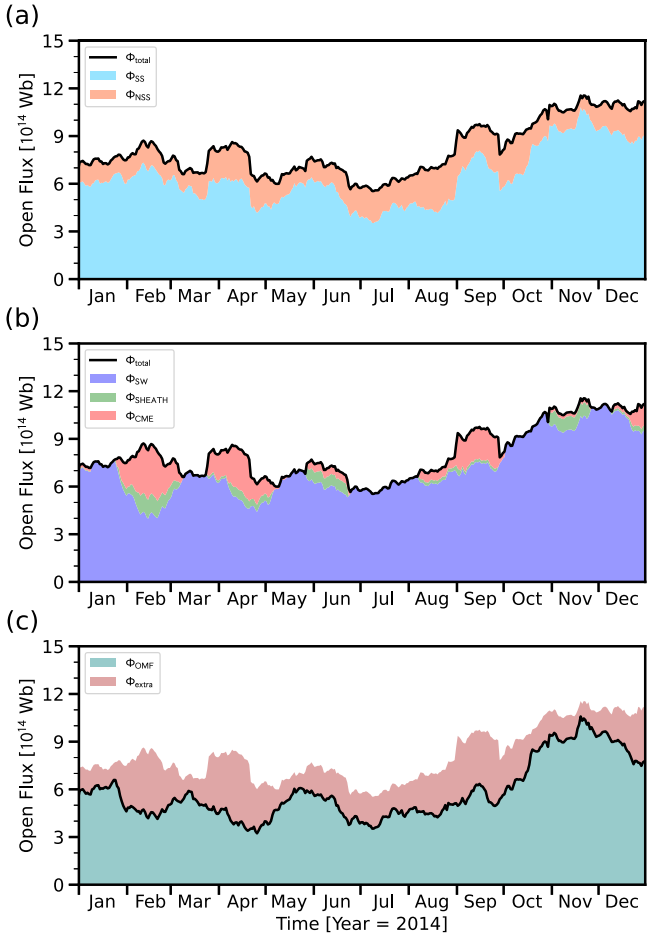

Figure 2. Estimated OMF from in situ measurements for 2014. Panel (a) shows the contributions of source-surface-connected (blue) and locally inverted flux (orange). In panel (b) the contributions of ambient solar wind (SW; blue), CME sheath region (green), and CME magnetic flux rope (red) are shown. Panel (c) details the part of the OMF that is connected to the Sun and has no CME contribution (Φ_{OMF}; teal) as well as the contribution from "extra" flux (i.e., locally inverted and CME flux; red).

Frost et al. (2022) used this method to separate the calculated open flux into source-surface-connected (Φ_{SS}) and non-source-surface-connected (Φ_{NSS}) flux. Topologies are estimated by combining the strahl and heliospheric magnetic field directions, and a direct source-surface connection is assumed if the strahl is (locally) moving antisunward, while an inverted interplantary magnetic field is indicated when the strahl is (locally) moving sunward. The non-source-surface-connected flux encompasses structures like large-scale magnetic field kinks (Kahler et al. 1996; Crooker et al. 2004), and small-scale structures like "switchbacks" (e.g., Dudok de Wit et al. 2020; Squire et al. 2020) and waves/turbulent eddies. For 2014, we find that on average 22% of the estimated flux is not connected to the Sun, with the contribution varying between 6% and 40% (see Figure 2(a)). As CMEs erupt in dynamic processes from the Sun, which are not captured in the magnetograms, and moreover might still be rooted at the Sun while propagating in heliospheric space, we want to exclude their contribution from the open flux calculation. We use the catalog for interplanetary coronal mass ejections (ICMEs) by Richardson

and Cane (Richardson & Cane 2010) to identify sheath regions and magnetic flux ropes. The magnetic flux rope intervals are removed and replaced with the 27 days average of the respective rotation. The same was done for the sheath region of the CME. The contributions of the different structures, i.e., ambient solar wind, compressed solar wind (sheath), and CME flux rope, to the calculated OMF are shown in Figure (2(b)). For the year of interest, 2014, we find that CMEs contribute up to 38% of the estimated flux and 9% on average. Respectively, the sheath regions contribute up to 14% and on average 3.5%. Temmer et al. (2021) showed that CME sheath regions are primarily made up of piled-up solar wind (see also Kilpua et al. 2017; Owens 2018) and, following this, we do not remove the contribution of the sheath region to the OMF.

By separating the different components of the derived OMF, we isolate the source-surface-connected contribution excluding the contribution from ICMEs, denoted as Φ_{OMF} (shown in Figure 2(c), teal curve). The locally inverted (i.e., non-source-surface-connected) and ICME-related contribution varies between 8% and 57%, and on average makes up 29% of the OMF in the 2014 time period. This immediately allows us to conclude that the strong rise around September–October cannot be explained by such "extra" contributions.

To evaluate whether the values derived for the year 2014 are representative in comparison to a longer time range, we extend the OMF calculations to the time period 1995–2022 covering solar cycles 23 and 24. We find that, on average, over these 27 yr 26% of the OMF is not connected to the Sun. This contribution varies between 3% and 57%. The magnetic structure of CMEs makes up 7% but can contribute up to 56%. During the 1999–2003 solar maximum, CMEs contributed up to 56% and on average 14%, and the following 2012–2016 maximum shows a lower contribution, with up to 38% and 9% on average. In contrast, during times of low solar activity, the average contribution of CMEs to the OMF is significantly lower, at a value of 5%. In summary, we find that the non-source-surface-connected and CME-related contributions vary between 5% and 77%, and on average make up 31% of the OMF. This total percentual contribution of "extra" flux is more or less constant and does not vary significantly with activity, but the intrinsic variation can be relatively high.

3. Results

We analyzed the evolution of the solar magnetic field in 2014 to unravel the source of the steep increase in OMF around September–October of the same year. By combining multiple data and processing techniques, we obtained the following results.

3.1. Timelines

In Figure 3, we present the OMF, detected coronal hole areas, open flux derived from the coronal holes, open flux derived using PFSS modeling, total unsigned flux from the used magnetograms, and the hemispheric sunspot numbers (Source: WDC-SILSO, Royal Observatory of Belgium, Brussels; SILSO World Data Center 1995–2022). We focus on the relevant time period between June, where the OMF has its minimum in 2014 (irrespective of the method of estimation), and December, which is after the peak in the OMF. The computed magnetic flux profiles using the various magnetograms agree well and

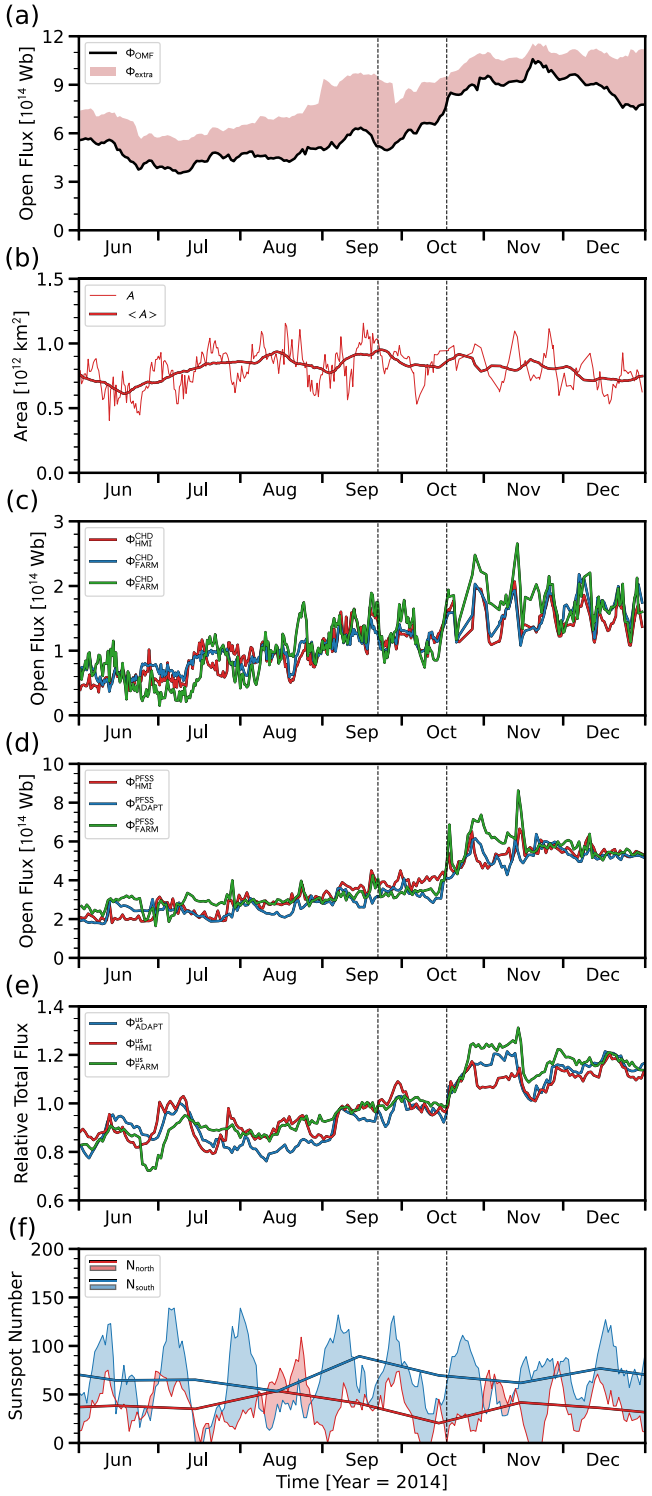

Figure 3. Evolution of the solar magnetic flux and related properties in 2014. Panel (a) shows the OMF, with the "extra" non-source-surface flux marked as the red shaded area. Panels (b) and (c) show the coronal hole area and the corresponding projected total open (signed) flux, respectively. In panel (d) the average PFSS calculated total open flux (from six source-surface heights) is given followed by panel (e), which shows the total unsigned magnetogram flux relative to the yearly mean. Lastly, in panel (f) the daily hemispheric sunspot number is presented with the monthly sunspot number overlaid. Panels (c)–(e) show the results as function of magnetogram used (red, HMI; blue, ADAPT; green, FARM). The vertical dashed black lines highlight the first emergence and the subsequent rotation into Earth's field of view of the largest active region in solar cycle 24 on around September 22 and October 18, respectively.

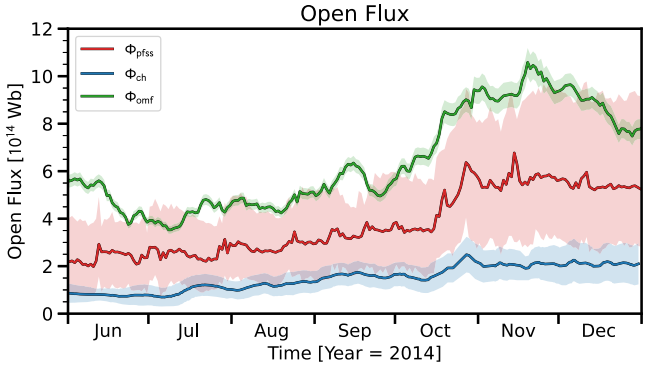

Figure 4. Open flux from different sources as function of time. The in situ calculated heliospheric open flux is shown in green. The average PFSS open flux calculated from the three different magnetograms and six source-surface heights is shown in red. The shaded area shows the uncertainty range, where the upper and lower boundaries are the flux calculated with $R_{ss} = 3.1$ and 1.5, respectively. The average open flux calculated from coronal hole observation overlaid on the three magnetograms is shown in blue, with the standard deviation between these three showing the uncertainty range due to different magnetograms (blue shaded area).

demonstrate the following behavior. In the OMF, we find a slow rising trend between June and September from 4 to 5×10^{14} Wb, followed by a rise to 10×10^{14} Wb within less than 2 months (Figure 3(a)). In Figure 3(b), the CHMAP coronal hole area as a function of time is shown. Before September, we find that the area rises from around 7 to 10×10^{11} km^2 from June to mid July, thereafter remaining mostly constant around 8 to 9×10^{11} km^2 before eventually slowly decreasing to around 7×10^{11} km^2 in December. The variation in the coronal hole area is not correlated with the rise in the OMF ($cc_{\mathrm{Pearson}} = 0.00$ $\mathrm{CI}_{95\%} = [-0.14, 0.14]$) between June and October. However, it should be noted that the total coronal hole area was found to be dependent on resolution (Caplan et al. 2021), which may alter the correlation. When considering the coronal hole open flux instead (Figure 3(c)), we find a continuous rise in open flux between 6×10^{13} Wb in June to up to 2×10^{14} Wb in November. The rise is much more continuous than the sudden jump in the OMF (although correlated $cc_{\mathrm{Pearson}} = 0.88$ $\mathrm{CI}_{95\%} = [0.85, 0.91]$) and coincides with the continuous growth of a large southern near-polar coronal hole whose signed flux increased by a factor of 3–4 from $\approx 3 \times 10^{13}$ Wb to $\approx 1.1 \times 10^{14}$ Wb in the same time period. This coronal hole contains up to 50% of the open flux originating from the observed coronal holes.

Figure 3(d) shows the total source-surface open flux as calculated using a PFSS model. Although the average values (mean of the previously mentioned six different source-surface solutions; see Equation (3)) are about a factor of 2 lower than the OMF (see Linker et al. 2017, for information on the open flux problem), the temporal evolution shows a well-correlated trend ($cc_{\mathrm{Pearson}} = 0.94$ $\mathrm{CI}_{95\%} = [0.92, 0.95]$) with the OMF. We find a slow rise between June and September from 2.5 to 3.5×10^{14} Wb, followed by a jump to 5×10^{14} Wb within a month. In Figure 4, we show that even when lowering the source-surface height in the model to an extremely low $1.5\,R_{\odot}$ (Asvestari et al. 2019), the OMF magnitude can barely be explained. Figure 3(e) shows the total unsigned magnetic flux of the synoptic magnetograms. Note that the total unsigned magnetic flux is highly dependent on resolution, and thus calculated for the same resolution and plotted relative to its mean value over the time period. We find that the total unsigned magnetic field increases continuously from July to October by roughly 20%, before rapidly increasing by another 20%–25% at the beginning of October. This trend is strongly correlated with the open flux calculated from the PFSS model ($cc_{\mathrm{Pearson}} = 0.94$ $\mathrm{CI}_{95\%} = [0.93, 0.96]$) as well as from coronal holes ($cc_{\mathrm{Pearson}} = 0.88$ $\mathrm{CI}_{95\%} = [0.85, 0.91]$). The correlation with the OMF is also high ($cc_{\mathrm{Pearson}} = 0.87$ $\mathrm{CI}_{95\%} = [0.84, 0.90]$). Lastly, in Figure 3(f) the hemispheric sunspot number shows an increase in activity at the beginning of 2014, while an overall decrease is observed during the September–October period in 2014. This is seemingly in contrast to the fact that the largest active region in solar cycle 24 emerged around September 2014. Additionally, we note a slight time lag of 2–3 days between the in-situ-measured and remote-sensing-observed OMFs. However, this does not significantly impact the correlation coefficient in this study.

The onset of the steep rise in the OMF coincides with the first appearance of the largest active region observed in solar cycle 24 (NOAA identifier number 12192) on September 22 in the southern hemisphere, which significantly grew until it rotated into Earth's field of view one rotation later on October 18. The second appearance coincides with the large jump in magnetic flux observed in the open flux calculated from coronal holes, from the PFSS model as well as with the unsigned total magnetic flux calculated from the magnetograms (Figures 3(a)–(e)). During its disk passage on October 18–30, there is only one eruptive event and CME reported from that active region, which happened on October 24 (see Thalmann et al. 2015).

In Figure 4, the OMF over time calculated from the coronal holes, the PFSS model, and in situ observations is shown. There is a large difference in magnitude between the results, however the general trend seems to agree even though the onset and following strength of the rise varies. Regardless, all three results show a plateau-like maximum starting from mid-October. Note that the OMF is calculated within 27 days intervals and, as a result, the observed 27 days periodicity is introduced through the utilization of a rolling window. Interestingly, and in contrast to the general understanding of the origin of the open flux, we find that the contribution of open flux that has its origin in coronal holes is only 14%–32% of the open flux measured in the heliosphere and 26%–55% of the average open flux derived from PFSS (further depending on source-surface height). The PFSS derived open flux is about 60% (between 36% and 76%) of the in situ measured one (in agreement with Linker et al. 2017).

3.2. Complexity of Solar Evolution

In the previous section, we explored how the Sun's global magnetic field properties evolved over time. Changes in the spatial distribution of the photospheric field, however, may not be discerned by reducing the state down to a single value. To evaluate the possible role of such spatial changes, Figure 5 shows the longitudinal mean magnetic field from daily HMI charts as a function of time. Below 30° latitude ($\sin(\lambda_{30^\circ}) = 0.5$) strong magnetic fields associated with active regions are visible. In the southern hemisphere, starting around April–May, a poleward motion of negative-polarity flux can be observed. This poleward motion of flux seems to be in the order of—if not slightly faster than—the meridional surface flows (Liang et al. 2018; meridional flow profile derived from helioseismology that takes inflows around active regions into

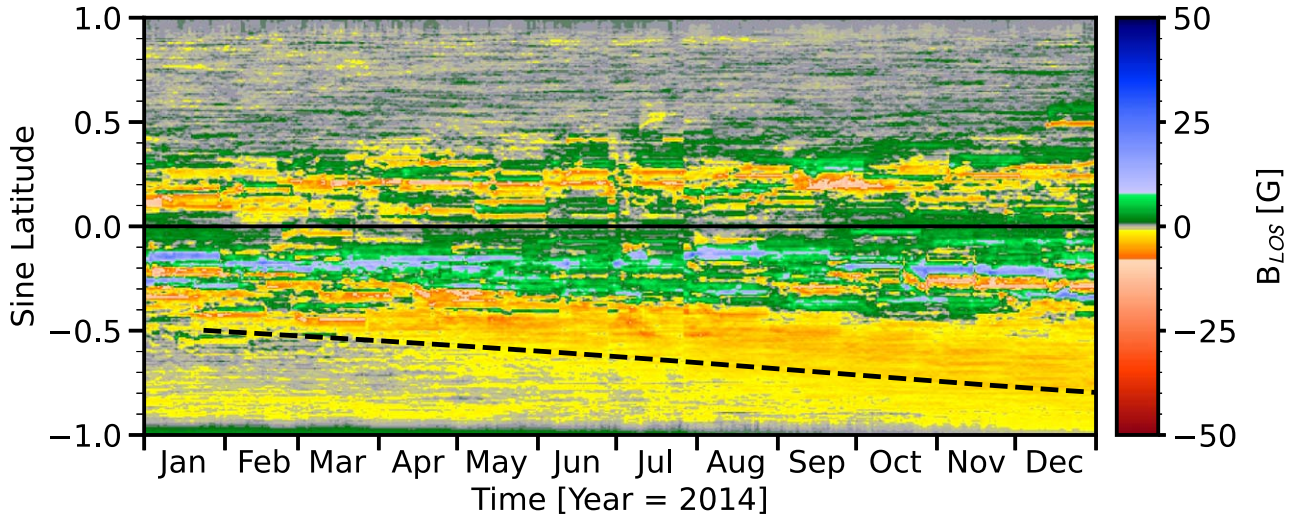

Figure 5. Longitudinally averaged magnetic field from daily HMI charts as a function of time. Each column on the time axis represents the longitudinal mean as function of latitude. The black dashed line represents a plasma or flux parcel moving polewards due to solar meridional flows.

account). The southern polar field still features a positive remnant field from the previous cycle, crowned by an accumulation of negative flux, which observationally coincides with a large, near-polar coronal hole. Due to the opposite-polarity flux migration to the pole and the associated increase in flux of the coronal hole, the remnant polar field decreases and seems to vanish around September–October. This is in good temporal agreement with the jump in the measured OMF. Note that the observed polar fields are notoriously unreliable due to the large line-of-sight projections. The southern polar magnetic field (defined as the mean field from latitudes $< -60°$) is increasing in magnitude from ≈ -0.1 G in June to > -1 G in December. The temporal evolution is correlated with the evolution of the OMF ($cc_{\mathrm{Pearson}} = 0.84$ $\mathrm{CI}_{95\%} = [0.79,\ 0.88]$) during this time period. The northern pole shows no significant change in magnetic field density.

The poleward motion of the remnant magnetic field from decaying active regions is also in agreement with the observed hemispheric sunspot number (Figure 6). Around 2014 January, a large disparity between the southern and northern hemispheric sunspot number can be observed, with the former exceeding the latter by nearly 90, or more than a factor 3. This strong asymmetry then decreases along with the total sunspot number, which indicates that a lot of active regions in the southern hemisphere decayed during that time. This is also observed in EUV (not shown here).

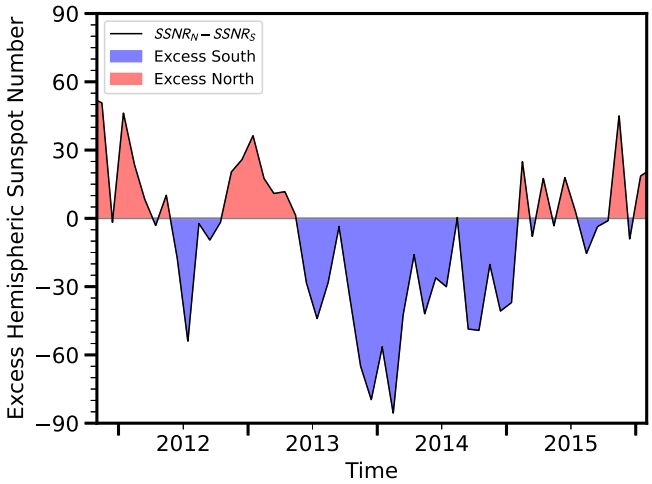

Figure 6. Excess hemispheric sunspot number over time for 2012–2016.

4. Discussion and Summary

In this study, we showed that the sudden rise in OMF is correlated with the evolution of the open flux calculated and modeled from remote-sensing observations. It temporally coincides with the decay of the remnant polarity in the southern hemisphere and the consequent increase in the OMF of the southern polar coronal hole. Yoshida et al. (2023) found that the peak in the OMF is synchronous with a sudden enhancement of equatorial dipole flux derived from a PFSS extrapolation model, which is in agreement with decaying active regions moving polewards.

The southern active region with NOAA number 12192 was the largest active region observed in solar cycle 24 and the source of six X-class flares and more than 20 M-class flares in October 2014 (Sarkar & Srivastava 2018). Of the X-class flares, four were found to be confined (Thalmann et al. 2015; Baumgartner et al. 2018). From its first appearance in September, it grew in size over 6 times to its appearance at the next solar rotation (Sarkar et al. 2018), which coincides with the largest jump in the observed OMF as well as in the flux derived from remote-sensing observations. The emergence of this active region seemed to have caused additional flux to open. Figure 7 shows the changes in the open magnetic field structure between October 23, when the active region was at its largest and in the center of Earth's field of view, and two rotations prior, when the active region had not yet emerged. Although there was no significant reconfiguration of the open field structure, an additional 41% of the open field area was observed, which increased the flux by over 50%. This is concurrent with a 25% increase in the total unsigned magnetogram flux in just two solar rotations (for the given HMI magnetogram at a resolution of 180×360 pixels and a source-surface height of $R_{\mathrm{SS}} = 2.1\ R_{\odot}$).

Note that magnetograms are subject to scaling and intercalibration to account for differences in observation technique, resolution, sensitivity, Stokes inversion, and

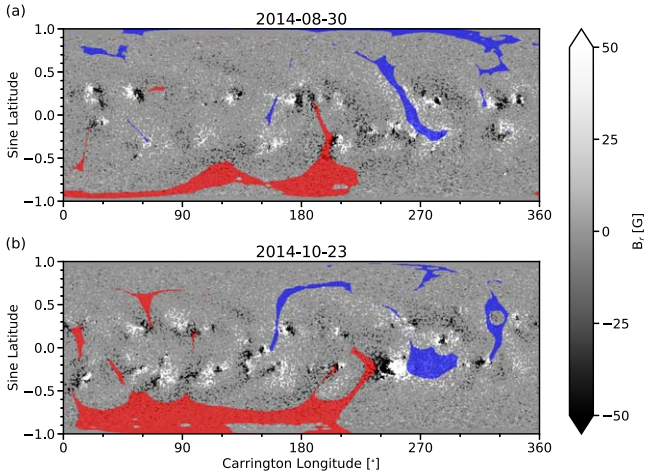

Figure 7. HMI synoptic charts from August 30 and October 22 with open field footpoints overlaid. The PFSS calculations were done at a resolution of 180×360 pixels, at a source-surface height of $R_{SS} = 2.1\ R_{\odot}$, and the field lines were traced to a lower boundary of $R = 1.03\ R_{\odot}$.

processing of the available data. For example, correction factors of $B_{scale} = 1.866$ and $B_{scale} = 1.35$ are used for HMI-ADAPT (depending on the time period and input data) to minimize offsets between different ADAPT maps. Pietarila et al. (2013) discovered a scaling factor between Vector Spectro-Magnetograph data from the Synoptic Optical Long-term Investigations of the Sun, and HMI magnetograms might be a nonlinear function of magnetic flux density, with values ranging from approximately 1 in regions of low magnetic flux density to about 1.5 in regions of high magnetic flux density. Therefore, the magnitudes of the magnetic flux calculated from remote-sensing observations (e.g., coronal hole flux or PFSS flux in this study) are subject to considerable uncertainty that is challenging to assess. However, examining the ratios and trends can offer valuable insights into the evolution of the interplanetary magnetic field structure and its sources. Wang et al. (2022b) attributes most of the missing open flux to the systematic underestimation of the observed magnetogram flux, contending that addressing this issue correctly can explain the open flux problem.

Our results of the open flux derived from PFSS, coronal holes, and in situ measurements confirm the long-standing open flux problem (Linker et al. 2017). Notably, in deviation from the prevailing notion regarding the source of open flux, our findings reveal that the open flux originating from coronal holes accounts for just 14%–32% of the total open flux detected within the heliosphere and 26%–55% of the open flux derived from PFSS. This aligns with the following simple theoretical deliberations: Considering that the average magnetic field density or field strength of a coronal hole amounts to 3 G (Bohlin & Sheeley 1978; Obridko & Shelting 1989; Belenko 2001), then coronal holes have to cover more than 50% of the solar surface to produce the observed 1×10^{15} Wb of open flux. However, large coronal holes (that according to the prevailing notion should contain the majority of the flux) usually have a lower magnetic field density of around 2.5 G (Heinemann et al. 2019b; Hofmeister et al. 2019), which means that more than two-thirds of the Sun would need to be covered by coronal holes to explain the observed open flux. Please note that we treat polar coronal holes based on the statistics derived from nonpolar coronal holes, potentially overlooking differences in their magnetic field density distribution. Furthermore, this argument overlooks the potential existence of small-scale coronal holes in proximity to active regions, where field strengths exceeding 20 G could be present but might be obscured by the complexity of the active corona (as suggested by Wang & Ko 2019). It appears that the presented results, along with the theoretical argument, suggest that the underdetection of what are traditionally referred to as coronal holes cannot resolve the discrepancy between the open flux observed from coronal holes and that derived from a PFSS model.

There is strong evidence that solar activity evolves differently in the northern and southern hemispheres (Temmer et al. 2002; Hathaway 2015; Lockwood et al. 2017) and that the coupling between the photosphere and the corona also varies over the 22 yr magnetic cycle (Wheatland & Litvinenko 2001). This is supported by the findings that strong flare activity on average is delayed during odd-numbered cycles with respect to the relative sunspot number (Temmer et al. 2003). The Gnevyshev gap, observed in sunspot number records during the solar cycle maximum, signals the magnetic field reversal and appears to happen separately in both hemispheres (Temmer et al. 2006). Janardhan et al. (2018) found that the global magnetic field reversal process was completed only in 2014 November for solar cycle 24 (which is also the peak of the open flux in our study), when the northern hemisphere had finished its final reversal. Wang et al. (2022a) point out that a significant portion of the OMF might come from low-latitude regions relating to magnetic field that stays open in the wake of CMEs (see also Luhmann et al. 1998). Likewise, a lag in the open flux with an even–odd cyclic behavior was reported by Owens et al. (2021).

Based on our results, we can attribute the large jump in heliospheric OMF around 2014 September–October, where it increased by over a factor of two within less than two months from 5×10^{14} Wb to 10×10^{14} Wb, to an interaction of different factors, which can be summarized as follows:

1. The strong increase in the OMF is well correlated with the PFSS-modeled magnetic field on the Sun ($cc_{Pearson} = 0.94$ $CI_{95\%} = [0.92, 0.95]$) and the open flux derived from solar coronal holes ($cc_{Pearson} = 0.88$ $CI_{95\%} = [0.85, 0.91]$). While the flux associated with coronal holes is well correlated, their total area is not.
2. A large coronal hole near the southern pole was found, whose open flux increased by a factor of 3–4 and that contains up to 50% of the total open flux derived from coronal holes on the Sun. This finding suggests a potential link between the coronal hole and the observed increase in OMF, although further investigation is required to establish a conclusive relationship.
3. Temporally, the sudden rise in OMF coincides with the disappearance of the remnant magnetic field at the southern pole, attributed to poleward flux circulations induced by the decay of a substantial number of active regions in the southern hemisphere a few months earlier. This temporal coincidence implies a connection between the decay of active regions and the subsequent increase in OMF.
4. Lastly, we find that the strong jump in the OMF may be related to the concurrent emergence of the largest active region of solar cycle 24, which had its greatest extension in October 2014.

On the short (i.e., subsolar cycle) timescales considered in this study, the OMFs estimated from in situ observations and photospheric extrapolations are highly correlated, though there is a systematic offset in the magnitudes (see also Linker et al. 2017). It has previously been shown that on longer timescales (i.e., cycle-to-cycle variations), this correlation breaks down (Wallace et al. 2019; Frost et al. 2022), possibly due to the systematic offset having a time-varying component. This suggests the presence of two distinct, decoupled sources of OMF, each operating on different timescales. Furthermore, a significant portion of this disparity may be attributed to the source regions of the "missing" open flux, which is unlikely to originate from the centers of observed coronal holes. Thus, to gain a comprehensive understanding of the Sun's magnetic structure and the heliosphere, additional efforts aimed at solving the open flux problem are imperative.

Acknowledgments

We thank the International Space Science Institute (ISSI, Bern) for the generous support of the ISSI team "Magnetic open flux and solar wind structuring in heliospheric space" (2019–2021). The SDO and STEREO image data are available by courtesy of NASA and the respective science teams. This research was funded in whole, or in part, by the Austrian Science Fund (FWF) Erwin-Schrödinger fellowship J-4560. S.G.H. expresses sincere thanks to Yi-Ming Wang for inspiring and fruitful discussions. The ADAPT model development is supported by Air Force Research Laboratory (AFRL), along with AFOSR (Air Force Office of Scientific Research) tasks 18RVCOR126 and 22RVCOR012. The views expressed are those of the authors and do not reflect the official guidance or position of the United States Government, the Department of Defense (DoD) or of the United States Air Force. M.O. is part funded by Science and Technology Facilities Council (STFC) grant No. ST/V000497/1. M.M. acknowledges DFG grant Nos. WI 3211/8-1 and 3211/8-2, project number 452856778, and was partially supported by the Bulgarian National Science Fund, grant No. KP-06-N44/2. J.P. acknowledges funding from the Academy of Finland project SWATCH (343581). R.P. acknowledges financial support by EU H2020 grant No. 870437 and by ERC (SLOW–SOURCE–DLV–819189). E.A. acknowledges support from the Academy of Finland/Research Council of Finland (Academy Research Fellow grant No. 355659). C.N.A. is supported by the NASA competed Heliophysics Internal Scientist Funding Model (ISFM). R.C., C.D., and J.A.L. of Predictive Science were supported by NASA grant Nos. 80NSSC22K0893, 80NSSC19K0273, and NSF grant ICER 1854790.

ORCID iDs

Stephan G. Heinemann https://orcid.org/0000-0002-2655-2108
Mathew J. Owens https://orcid.org/0000-0003-2061-2453
Manuela Temmer https://orcid.org/0000-0003-4867-7558
Charles N. Arge https://orcid.org/0000-0001-9326-3448
Carl J. Henney https://orcid.org/0000-0002-6038-6369
Jens Pomoell https://orcid.org/0000-0003-1175-7124
Eleanna Asvestari https://orcid.org/0000-0002-6998-7224
Jon A. Linker https://orcid.org/0000-0003-1662-3328
Cooper Downs https://orcid.org/0000-0003-1759-4354
Ronald M. Caplan https://orcid.org/0000-0002-2633-4290
Stefan J. Hofmeister https://orcid.org/0000-0001-7662-1960
Camilla Scolini https://orcid.org/0000-0002-5681-0526
Rui F. Pinto https://orcid.org/0000-0001-8247-7168
Maria S. Madjarska https://orcid.org/0000-0001-9806-2485

References

Abbo, L., Ofman, L., Antiochos, S. K., et al. 2016, SSRv, 201, 55
Acuña, M. H., Ogilvie, K. W., Baker, D. N., et al. 1995, SSRv, 71, 5
Altschuler, M. D., & Newkirk, G. 1969, SoPh, 9, 131
Anderson, B. R., Skoug, R. M., Steinberg, J. T., & McComas, D. J. 2012, JGRA, 117, A04107
Antiochos, S. K., Mikić, Z., Titov, V. S., Lionello, R., & Linker, J. A. 2011, ApJ, 731, 112
Arge, C. N., Henney, C. J., Hernandez, I. G., et al. 2013, in AIP Conf. Ser. 1539, ed. G. P. Zank et al. (Melville, NY: AIP), 11
Arge, C. N., Leisner, A., Antiochos, S. K., Wallace, S., & Henney, C. J. 2024, ApJ, 964, 115
Asvestari, E., Heinemann, S. G., Temmer, M., et al. 2019, JGRA, 124, 8280
Bale, S. D., Badman, S. T., Bonnell, J. W., et al. 2019, Natur, 576, 237
Barnes, G., DeRosa, M. L., Jones, S. I., et al. 2023, ApJ, 946, 105
Baumann, I. J. 2005, PhD thesis, Univ. Göttingen
Baumgartner, C., Thalmann, J. K., & Veronig, A. M. 2018, ApJ, 853, 105
Belenko, I. A. 2001, SoPh, 199, 23
Bohlin, J. D. 1977, SoPh, 51, 377
Bohlin, J. D., & Sheeley, N. R., Jr 1978, SoPh, 56, 125
Caplan, R. M., Downs, C., Linker, J. A., & Mikic, Z. 2021, ApJ, 915, 44
Caplan, R. M., Downs, C., & Linker, J. A. 2016, ApJ, 823, 53
Caplan, R. M., Mason, E. I., Downs, C., & Linker, J. A. 2023, ApJ, 958, 43
Cranmer, S. R. 2009, LRSP, 6, 3
Crooker, N. U., Kahler, S. W., Larson, D. E., & Lin, R. P. 2004, JGRA, 109, A03108
Doschek, G. A., Warren, H. P., Mariska, J. T., et al. 2008, ApJ, 686, 1362
Dudok de Wit, T., Krasnoselskikh, V. V., Bale, S. D., et al. 2020, ApJS, 246, 39
Fisk, L. A., Schwadron, N. A., & Zurbuchen, T. H. 1998, SSRv, 86, 51
Frost, A. M., Owens, M., Macneil, A., & Lockwood, M. 2022, SoPh, 297, 82
Gosling, J. T., McComas, D. J., Phillips, J. L., & Bame, S. J. 1992, JGR, 97, 6531
Harra, L. K., Sakao, T., Mandrini, C. H., et al. 2008, ApJL, 676, L147
Hathaway, D. H. 2015, LRSP, 12, 4
Heinemann, S. G., Jerčić, V., Temmer, M., et al. 2020, A&A, 638, A68
Heinemann, S. G., Temmer, M., Farrugia, C. J., et al. 2019b, SoPh, 294, 121
Heinemann, S. G., Temmer, M., Heinemann, N., et al. 2019a, SoPh, 294, 144
Heinemann, S. G., Temmer, M., Hofmeister, S. J., et al. 2021, SoPh, 296, 141
Hewins, I. M., Gibson, S. E., Webb, D. F., et al. 2020, SoPh, 295, 161
Hickmann, K. S., Godinez, H. C., Henney, C. J., & Arge, C. N. 2015, SoPh, 290, 1105
Hoeksema, J. T. 1984, PhD thesis, Stanford Univ.
Hofmeister, S. J., Utz, D., Heinemann, S. G., Veronig, A., & Temmer, M. 2019, A&A, 629, A22
Hofmeister, S. J., Veronig, A., Reiss, M. A., et al. 2017, ApJ, 835, 268
Janardhan, P., Fujiki, K., Ingale, M., Bisoi, S. K., & Rout, D. 2018, A&A, 618, A148
Kahler, S. W., Crooker, N. U., & Gosling, J. T. 1996, JGR, 101, 24373
Kaiser, M. L., Kucera, T. A., Davila, J. M., et al. 2008, SSRv, 136, 5
Kilpua, E., Koskinen, H. E. J., & Pulkkinen, T. I. 2017, LRSP, 14, 5
Lemen, J. R., Title, A. M., Akin, D. J., et al. 2012, SoPh, 275, 17
Lepping, R. P., Acũna, M. H., Burlaga, L. F., et al. 1995, SSRv, 71, 207
Liang, Z.-C., Gizon, L., Birch, A. C., Duvall, T. L., & Rajaguru, S. P. 2018, A&A, 619, A99
Lin, R. P., Anderson, K. A., Ashford, S., et al. 1995, SSRv, 71, 125
Linker, J. A., Caplan, R. M., Downs, C., et al. 2017, ApJ, 848, 70
Linker, J. A., Heinemann, S. G., Temmer, M., et al. 2021, ApJ, 918, 21
Lockwood, M., Owens, M. J., Imber, S. M., et al. 2017, JGRA, 122, 5870
Luhmann, J. G., Gosling, J. T., Hoeksema, J. T., & Zhao, X. 1998, JGR, 103, 6585
Macneil, A. R., Owens, M. J., Berčič, L., & Finley, A. J. 2020, MNRAS, 498, 5273
McComas, D. J., Bame, S. J., Barker, P., et al. 1998, SSRv, 86, 563
McGregor, S. L., Hughes, W. J., Arge, C. N., & Owens, M. J. 2008, JGRA, 113, A08112
Obridko, V. N., & Shelting, B. D. 1989, SoPh, 124, 73
Ofman, L. 2004, AdSpR, 33, 681

Owens, M. J. 2018, SoPh, 293, 122
Owens, M. J., & Forsyth, R. J. 2013, LRSP, 10, 5
Owens, M. J., Lockwood, M., Barnard, L. A., & MacNeil, A. R. 2018, ApJL, 868, L14
Owens, M. J., Lockwood, M., Barnard, L. A., et al. 2021, SoPh, 296, 82
Owens, M. J., Lockwood, M., Riley, P., & Linker, J. 2017, JGRA, 122, 10
Pagel, C., Crooker, N. U., & Larson, D. E. 2005, GeoRL, 32, L14105
Pesnell, W. D., Thompson, B. J., & Chamberlin, P. C. 2012, SoPh, 275, 3
Pietarila, A., Bertello, L., Harvey, J. W., & Pevtsov, A. A. 2013, SoPh, 282, 91
Richardson, I. G., & Cane, H. V. 2010, SoPh, 264, 189
Riley, P., & Luhmann, J. G. 2012, SoPh, 277, 355
Sakao, T., Kano, R., Narukage, N., et al. 2007, Sci, 318, 1585
Samara, E., Magdalenić, J., Rodriguez, L., et al. 2022, A&A, 662, A68
Sarkar, R., & Srivastava, N. 2018, SoPh, 293, 16
Sarkar, R., Srivastava, N., & Dhara, S. K. 2018, in IAU Symp. 335, Space Weather of the Heliosphere: Processes and Forecasts, ed. C. Foullon & O. E. Malandraki (Cambridge: Cambridge Univ. Press), 32
Schou, J., Scherrer, P. H., Bush, R. I., et al. 2012, SoPh, 275, 229
SILSO World Data Center 1995-2022, International Sunspot Number Monthly Bulletin and Online Catalog, https://www.sidc.be/SILSO/
Skoug, R. M., Feldman, W. C., Gosling, J. T., McComas, D. J., & Smith, C. W. 2000, JGR, 105, 23069
Smith, C. W., L'Heureux, J., Ness, N. F., et al. 1998, SSRv, 86, 613
Squire, J., Chandran, B. D. G., & Meyrand, R. 2020, ApJL, 891, L2
Stansby, D., Matteini, L., Horbury, T. S., et al. 2020, MNRAS, 492, 39
Stone, E. C., Frandsen, A. M., Mewaldt, R. A., et al. 1998, SSRv, 86, 1
Suess, S. T., & Smith, E. J. 1996, GeoRL, 23, 3267
Suess, S. T., Smith, E. J., Phillips, J., Goldstein, B. E., & Nerney, S. 1996, A&A, 316, 304
Temmer, M. 2021, LRSP, 18, 4
Temmer, M., Holzknecht, L., Dumbović, M., et al. 2021, JGRA, 126, e28380
Temmer, M., Rybák, J., Bendík, P., et al. 2006, A&A, 447, 735
Temmer, M., Veronig, A., & Hanslmeier, A. 2002, A&A, 390, 707
Temmer, M., Veronig, A., & Hanslmeier, A. 2003, SoPh, 215, 111
Thalmann, J. K., Su, Y., Temmer, M., & Veronig, A. M. 2015, ApJL, 801, L23
Viall, N. M., & Borovsky, J. E. 2020, JGRA, 125, e26005
Wallace, S., Arge, C. N., Pattichis, M., Hock-Mysliwiec, R. A., & Henney, C. J. 2019, SoPh, 294, 19
Wang, Y., Guo, J., Li, G., Roussos, E., & Zhao, J. 2022a, ApJ, 928, 157
Wang, Y. M., & Ko, Y. K. 2019, ApJ, 880, 146
Wang, Y. M., Lean, J., & Sheeley, N. R. 2000, GeoRL, 27, 505
Wang, Y. M., & Sheeley, N. R. J. 1995, ApJL, 447, L143
Wang, Y.-M., & Sheeley, N. R., Jr 1990, ApJ, 355, 726
Wang, Y. M., Ulrich, R. K., & Harvey, J. W. 2022b, ApJ, 926, 113
Wheatland, M. S., & Litvinenko, Y. E. 2001, ApJ, 557, 332
Wuelser, J.-P., Lemen, J. R., Tarbell, T. D., et al. 2004, Proc. SPIE, 5171, 111
Yang, D., Gizon, L., & Barucq, H. 2023, A&A, 669, A89
Yang, D., Heinemann, S. G., Cameron, R., & Gizon, L. 2024, SoPh, submitted
Yoshida, M., Shimizu, T., & Toriumi, S. 2023, ApJ, 950, 156